

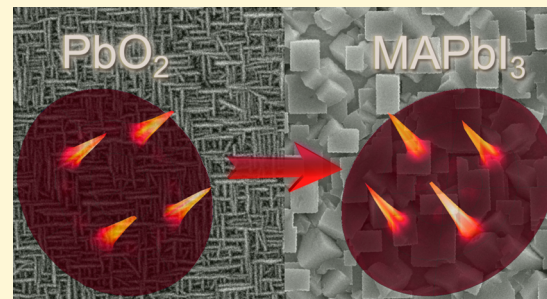
Epitaxial Electrodeposition of Methylammonium Lead Iodide Perovskites

Jakub A. Koza, James C. Hill, Ashley C. Demster, and Jay A. Switzer*

Department of Chemistry and Graduate Center for Materials Research, Missouri University of Science and Technology, Rolla, Missouri 65409, United States

S Supporting Information

ABSTRACT: An electrochemical/chemical route is introduced to deposit both textured and epitaxial films of methylammonium lead iodide (MAPbI_3) perovskites. The perovskite films are produced by chemical conversion of lead dioxide films that have been electrodeposited as either textured or epitaxial films onto [111]-textured Au and [100] and [111] single-crystal Au substrates. The epitaxial relationships for the MAPbI_3 films are $\text{MAPbI}_3(001)\text{-}[010]\|\text{PbO}_2(100)\langle 001 \rangle$ and $\text{MAPbI}_3(110)[111]\|\text{PbO}_2(100)\langle 001 \rangle$ regardless of the Au substrate orientation, because the in-plane order of the converted film is controlled by the epitaxial PbO_2 precursor film. The textured and epitaxial MAPbI_3 films both have trap densities lower than and photoluminescence intensities higher than those of polycrystalline films produced by spin coating.



INTRODUCTION

Methylammonium lead iodide (MAPbI_3) perovskites are efficient light harvesters in photovoltaic solar cells.^{1–7} Since their introduction as a light absorber in TiO_2 -based solar cells in 2009,¹ the conversion efficiency of perovskite-based photovoltaic cells increased from 3.8 to 20.1% in only four years.^{1,8} Although most research on perovskites has focused on producing polycrystalline films by simple and inexpensive solution processing methods,^{6,9–11} recent results have shown that large-grained materials and single crystals have lower trap densities, longer diffusion lengths, enhanced photoluminescence, and higher photovoltaic conversion efficiencies.^{12–16} In addition to producing higher efficiencies, highly ordered samples provide the opportunity to measure the intrinsic electronic and optical properties of the perovskites.¹⁷ An important next step in perovskite research is to grow the material as epitaxial films, in which the out-of-plane and in-plane orientation of the material is controlled by the substrate. Ordered microribbons of MAPbI_3 were deposited by Li et al. onto ST-cut quartz in which the orientation of the ribbons was templated by surface microgrooves of the quartz.¹⁸ Because the MAPbI_3 in that work consisted of randomly oriented polycrystalline microribbons, they do not appear to be crystallographically epitaxial.

Recently, we have shown that a vapor-assisted conversion of electrodeposited, epitaxial PbI_2 films leads to strongly textured MAPbI_3 films.¹⁹ However, the converted films did not show in-plane order but rather a fiber texture. Here, we introduce a simple, low-temperature electrochemical/chemical route to deposit both textured and epitaxial MAPbI_3 films on Au substrates. The perovskite films are produced by chemical conversion of lead dioxide films that have been electrode-

deposited as either textured or epitaxial films onto [111]-textured Au and [100] and [111] single-crystal Au substrates. The textured and epitaxial MAPbI_3 films have trap densities lower than and photoluminescence intensities higher than those of polycrystalline films produced by spin coating.

In addition to possible technological advantages of epitaxial MAPbI_3 films, the Au/ PbO_2 / MAPbI_3 system provides an interesting and unexpected example of epitaxy, in which an epitaxial film of PbO_2 on Au with large lattice mismatch is converted to an epitaxial film of MAPbI_3 by a simple dip conversion in solution. The electrodeposited PbO_2 crystallizes as the orthorhombic polymorph (space group $Pbcn$) with the following lattice parameters: $a = 0.4971$ nm, $b = 0.5956$ nm, and $c = 0.5438$ nm.²⁰ It is electrodeposited as an epitaxial film onto face-centered-cubic Au (space group $Fm\bar{3}m$) with $a = 0.40786$ nm.²⁰ PbO_2 is then chemically converted to tetragonal MAPbI_3 (space group $I4cm$) with the following lattice parameters: $a = 0.8849$ nm, and $c = 1.2641$ nm.^{17,21} Although there is a 515% increase in volume per Pb atom when PbO_2 is converted to MAPbI_3 , the MAPbI_3 maintains an in-plane and out-of-plane order that is determined by the PbO_2 . We have previously shown that electrodeposited ceramic films can grow epitaxially on large mismatch substrates through the formation of coincidence lattices.^{22–25}

EXPERIMENTAL SECTION

PbO₂ Electrodeposition. PbO_2 was electrodeposited from a solution of 0.1 M $\text{Pb}(\text{NO}_3)_2$ and 5 M NaOH in deionized (DI) water at 50 °C.²⁰ Films were deposited at a potential of 0.2 V on Au

Received: November 19, 2015

Published: December 16, 2015

sputtered glass and Au single crystals and at 0.25 V on Pt-sputtered quartz crystals using a Brinkmann PGSTAT 30 Autolab potentiostat. The change in mass during deposition and conversion experiments was monitored *in situ* with an electrochemical quartz crystal microbalance (EQCM, Stanford Research Systems QCM200). A stainless steel mesh served as the counter electrode. The electrodes were rinsed with concentrated HCl followed by DI water prior to each experiment to remove possible contaminants. Prior to being deposited, the single-crystalline Au substrates were electropolished in a 1:1:2 (by volume) 38% HCl/ethylene glycol/ethanol electrolyte at 55 °C at an anodic current density of 1.5 A cm⁻².²⁶ A Ag/AgCl/KCl_{sat} reference electrode was used in the deposition experiments.

Polymerized PbI₂ Film Synthesis. PbI₂ thin films were spin coated onto Au-coated glass substrates followed by annealing using a modified procedure reported by Burschka et al.⁶ PbI₂ was dissolved in N,N-dimethylformamide (DMF) to form a 0.5 M solution. The dissolution was performed at 70 °C, and the solution was kept at this temperature during the entire process. The film was spin coated at 2500 rpm for 30 s and then dried at 70 °C for 30 min.

CH₃NH₃I Synthesis. Methylammonium iodide (CH₃NH₃I, MAI) was synthesized through the reaction of HI with methylamine (CH₃NH₂) followed by crystallization.²⁷ An equimolar amount of HI was added to the 40% CH₃NH₂ at 0 °C while the sample was being stirred. The solution was stirred for ~2 h. Crystallization was achieved by evaporation at ~70 °C for 3 days. The product was rinsed with ethyl acetate (CH₃COOCH₂CH₃) and dried thoroughly.

PbO₂ and PbI₂ to CH₃NH₃PbI₃ Conversion. The electrodeposited PbO₂ films were converted to CH₃NH₃PbI₃ (MAPbI₃) by immersion in 0.1 M CH₃NH₃I in a 2-propanol solution. The electrode potential during the conversion was monitored using a Pt quasi reference electrode. The temperature of the solution was controlled with a thermostat (HAAKE DC10, K20). *In situ* mass changes during the conversion were measured with an EQCM for the PbO₂ films deposited onto a Pt-sputtered quartz crystal electrode. The spin-coated PbI₂ films were converted by immersion in 0.1 M CH₃NH₃I in 2-propanol at room temperature.

Characterization. The structure and texture of the films were determined using high-resolution Philips X-Pert MRD and MPD X-ray diffractometers (XRD) with a Cu K α_1 radiation source ($\lambda = 1.54056 \text{ \AA}$). The morphology of the films was studied by scanning electron microscopy (SEM) (Hitachi S-4700 FESEM and Helios Nanolab 600 FIB). Absorption spectra of MAPbI₃ films were measured using the diffuse reflectance option of a Varian CARY 5 UV-vis-NIR spectrophotometer. Photoluminescence spectra of MAPbI₃ films were run on a Horiba FL3-22 Fluorolog spectrofluorometer with an excitation wavelength of 480 nm.

Trap density measurements of the MAPbI₃ films were performed in a two-point, vertical geometry using a Keithley 2400 current source. A top contact to the film was made with a Au low-pressure pin. An electrical connection was made to the Au substrate, which served as the bottom contact. Experiments were performed in the dark.

RESULTS AND DISCUSSION

The reaction scheme used to produce MAPbI₃ films is shown in Figure 1. Lead dioxide films are electrodeposited anodically

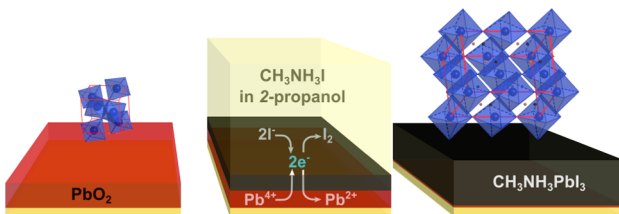


Figure 1. Reaction scheme used to produce MAPbI₃ films from electrodeposited PbO₂ by reaction with methylammonium iodide in 2-propanol.

from an aqueous solution of 0.1 M Pb(II) in 5 M NaOH at 50 °C using an applied potential of 0.2 V versus Ag/AgCl (Figure 1). The electrodeposited PbO₂ is then chemically converted in one step to MAPbI₃ by immersion in 0.1 M CH₃NH₃I in 2-propanol (Figure 1). Although Chen et al. have produced MAPbI₃ from electrodeposited tetragonal PbO₂, the polycrystalline MAPbI₃ films were randomly oriented.²⁸

The chemical conversion of PbO₂ to MAPbI₃ can be followed in real time using the electrochemical quartz crystal microbalance (EQCM) on polycrystalline substrates. This allows us to choose the appropriate conversion time and to determine the kinetics of the chemical conversion. Figure 2a

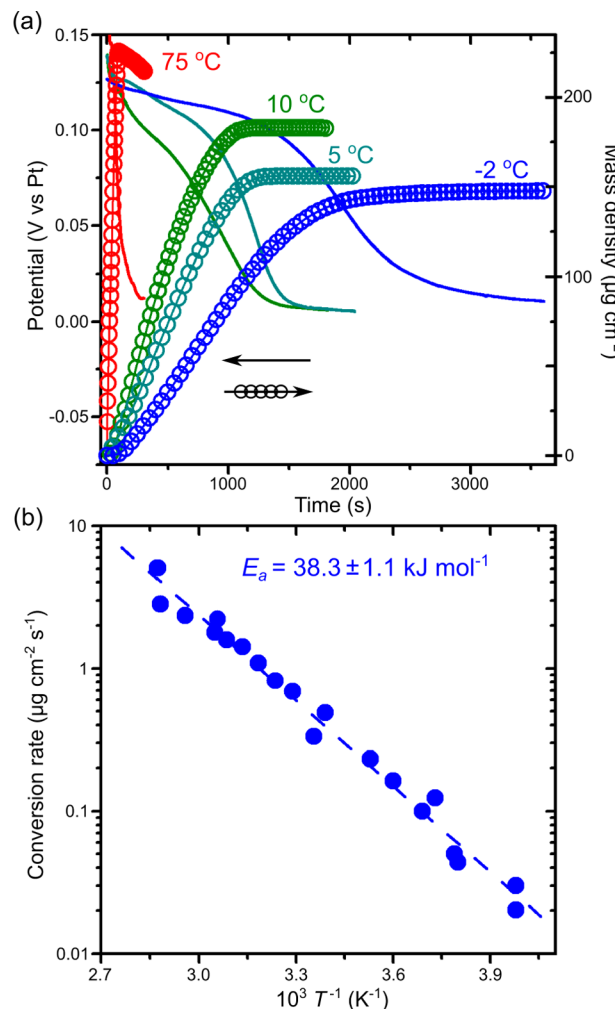


Figure 2. (a) Potential (lines, left axis) and mass density (circles, right axis) as a function of conversion time measured at different temperatures. (b) Arrhenius plot used to determine the activation energy (E_a) for conversion.

shows plots of the mass density gain and the open circuit potential as a function of time for the chemical conversion of PbO₂ to MAPbI₃ at temperatures from -2 to 75 °C. The rate of conversion increases as the temperature increases, and the MAPbI₃ film begins to dissolve when it is converted at higher temperatures. The temperature at which film dissolution becomes apparent is ~55 °C (Figure S1). The open circuit potential is also a good guide to the conversion process, because the mass increase and open circuit potential both

stabilize when the conversion is complete. In addition to providing feedback on the conversion process, the EQCM data can be used to determine the activation energy for the conversion process. The Arrhenius plot in Figure 2b yields a low activation energy of $38.3 \pm 1.1 \text{ kJ mol}^{-1}$, consistent with the observed fast conversion of PbO_2 to MAPbI_3 .

The MAPbI_3 perovskite grows with a fiber texture when deposited onto [111]-oriented Au-coated glass (Figure S2). Figure 3a shows X-ray diffraction (XRD) patterns of PbO_2

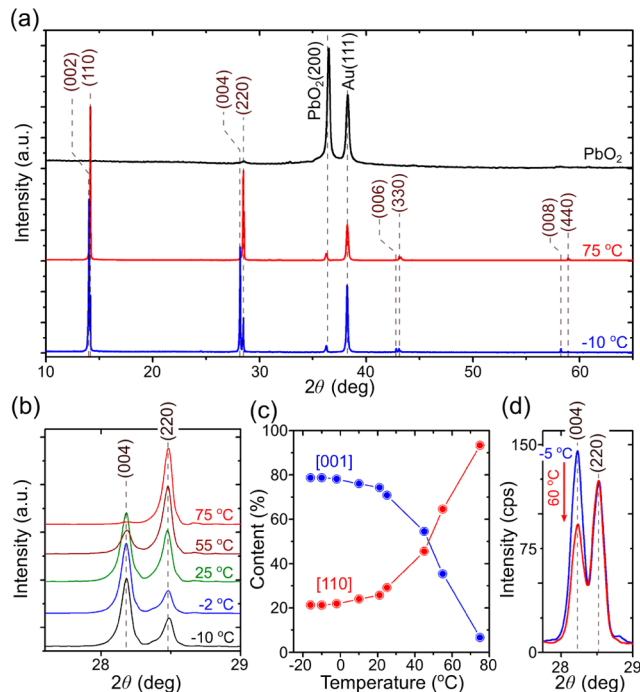


Figure 3. (a) XRD patterns of as-deposited PbO_2 (black) and a MAPbI_3 film converted at 75°C (red) and -10°C (blue) on Au-coated glass substrates. (b) XRD patterns of MAPbI_3 films converted on Au-coated glass substrates at different temperatures in the narrow (004)/(220) 2θ angle range. (c) Relative amounts of the [001] (blue) and [110] (red) out-of-plane orientations as a function of conversion temperature. (d) XRD patterns of a MAPbI_3 film converted on a Au-coated glass substrate at -5°C (blue) followed by a 10 min immersion in the conversion solution at 60°C (red).

deposited on the Au-coated glass and two perovskite films that were converted from electrodeposited PbO_2 at -10 and 75°C . The PbO_2 grows with a [100] fiber texture on the substrate, as described previously by Vertegel et al.²⁰ Only the (200) reflection of PbO_2 is observed in the XRD pattern. The orientation of the perovskite is a function of conversion temperature. The [001] orientation is favored for films that are converted at low temperatures, and the [110] orientation is favored for films converted at higher temperatures. XRD patterns for perovskite films showing only the (004) and (220) reflections are shown in Figure 3b for a series of temperatures. The relative amounts of the two orientations are shown in Figure 3c. At lower temperatures such as -10°C , the predominant orientation is [001] (approximately 80%), whereas at 75°C , only the [110] orientation is produced. Docampo et al. also observed that higher conversion temperatures favored the [110] orientation.²⁹ They observed a higher photovoltaic efficiency for a perovskite solar cell in which the perovskite was converted at 60°C and attributed the higher

efficiency to the anisotropic electronic properties of the perovskite.²⁹ One explanation for the preferred [110] orientation at higher conversion temperatures is the fact that the [001] orientation preferentially etches at the higher temperatures. The XRD patterns in Figure 3d are consistent with this argument. Figure 3d shows XRD patterns of an as-deposited film grown at -5°C and the same film that was immersed for 10 min in the conversion solution at 60°C . The intensity of the (004) reflection decreases after immersion in a hot solution, whereas the intensity of the (220) reflection is unchanged, consistent with preferential etching of the [001] orientation.

The MAPbI_3 perovskite grows with both out-of-plane and in-plane order when deposited onto single-crystalline Au(100) and Au(111) substrates. XRD patterns of electrodeposited PbO_2 and MAPbI_3 films converted at -10 and 75°C are shown in panels a and b of Figure 4, respectively. The PbO_2 deposits

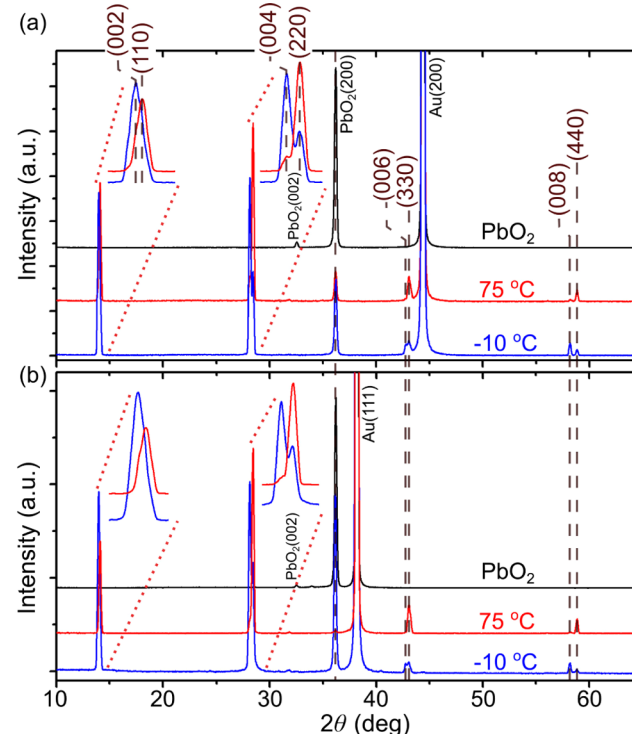


Figure 4. XRD patterns of as-deposited PbO_2 (black) and a MAPbI_3 film converted at 75°C (red) and -10°C (blue) deposited on (a) Au(100) and (b) Au(111) substrates.

with a [100] out-of-plane orientation on both substrates. After conversion, a thin interlayer of PbO_2 remains between the MAPbI_3 and Au (Figure S3). The converted MAPbI_3 films have either a [110] orientation or a [001] orientation, depending on the temperature of the conversion solution. Films converted at -10°C have predominately a [001] orientation, whereas films converted at 75°C have predominately a [110] orientation.

The in-plane order of the MAPbI_3 films is apparent in the X-ray pole figures (Figure 5). In a pole figure, planes other than those parallel with the substrate surface are probed by selecting the Bragg angle, θ , for the plane of interest and then tilting the sample through a series of tilt angles, χ , and rotating the sample through azimuthal angles, ϕ , from 0° to 360° . For films with in-plane order, peaks occur in the pole figure when the Bragg condition is satisfied, whereas for textured films with no in-

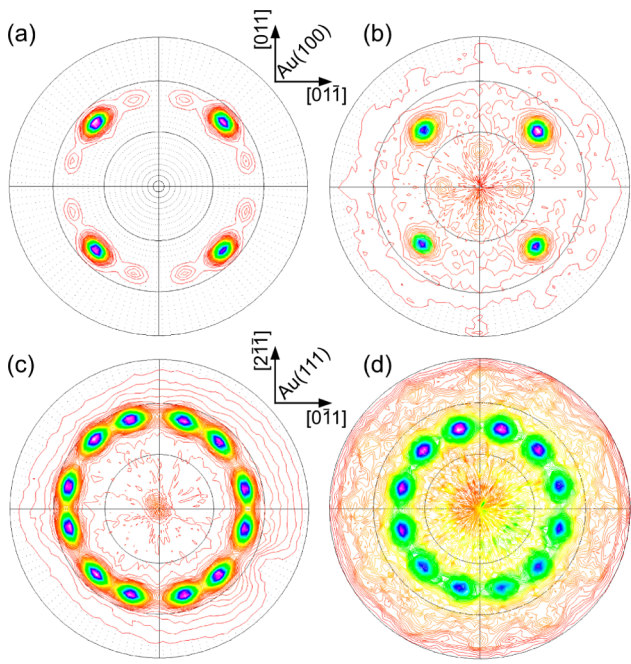


Figure 5. (a) (111) pole figure of electrodeposited PbO₂ on Au(100). (b) (224) pole figure of a MAPbI₃ film converted at 75 °C on Au(100). (c) (111) pole figure of electrodeposited PbO₂ on Au(111). (d) (224) pole figure of a MAPbI₃ film converted at 75 °C on Au(111).

plane order, rings are observed in the pole figure (Figure S2). Panels a and c of Figure 5 show (111) pole figures for PbO₂ electrodeposited onto Au(100) and Au(111) substrates. The PbO₂ pole figure shows 4-fold symmetry on Au(100) and 12-fold symmetry on Au(111) substrate, in agreement with the symmetries of the corresponding gold planes (see the Supporting Information for stereographic projections and details). The epitaxial relationships determined from the pole figures are PbO₂(100)[001]||Au(100)<011> and PbO₂(100)-[001]||Au(111)<211>. The (224) pole figures shown in panels b and d of Figure 5 for MAPbI₃ films on Au(100) and Au(111) converted at 75 °C show spots at a tilt angle of 45° in agreement with the angle between the (110) and (224) planes for the tetragonal MAPbI₃ structure. The in-plane orientation is controlled by the orientation of the precursor PbO₂ film (see the Supporting Information for stereographic projections and details). The films converted at lower temperatures also show spot patterns; however, the angle between the (110) and (224) planes (44.71°) is nearly identical with the angle between the (001) and (224) planes (45.25°), so no difference between the pole figures of the MAPbI₃ films converted at different temperatures was observed. The epitaxial relationships for the MAPbI₃ films were: MAPbI₃(001)[010]||PbO₂(100)<001> and MAPbI₃(110)[111]||PbO₂(100)<001> regardless of the Au substrate orientation, because the in-plane order of the converted film is controlled by the PbO₂ precursor film.

Interface models for the [110] and [001] orientations of MAPbI₃ on [100]-oriented PbO₂ that are consistent with the X-ray pole figures are shown in panels a and b of Figure 6. The interface models in panels a and b of Figure 6 show the Pb atoms of PbO₂ as red spheres and the Pb atoms of MAPbI₃ as blue spheres. For both the [001] orientation in Figure 6a and the [110] orientation in Figure 6b, the lowest mismatch is observed for a coincidence lattice with 3 × 8 unit meshes.

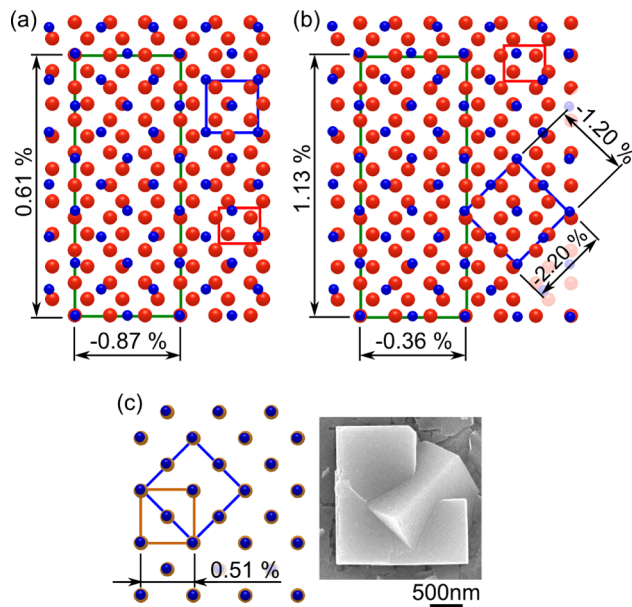


Figure 6. (a) Interface model of MAPbI₃(001) (blue) on PbO₂(200) (red). (b) Interface model of MAPbI₃(110) (blue) on PbO₂(200) (red). (c) Interface model of MAPbI₃(110) (blue) on MAPbI₃(001) (orange) showing a lattice mismatch of only 0.51%. The SEM image in panel c shows the intergrowth of two [110]- and [001]-oriented MAPbI₃ crystals obtained at 50 °C.

However, for the [110] orientation, a single unit mesh of MAPbI₃ fits the PbO₂(200) planes with only 2.2% lattice mismatch in the MAPbI₃[001] direction and -1.2% lattice mismatch in the MAPbI₃[110] direction. This suggests an energetic preference to deposit the [110] orientation of MAPbI₃ on PbO₂(100). Figure 6c shows an interface model for MAPbI₃(110) (blue) on MAPbI₃(001) (orange). There is only a 0.51% lattice mismatch between these two crystal planes of MAPbI₃, suggesting that the two orientations are likely to grow rotated 45° with respect to each other. The inset in Figure 6c shows such an intergrowth of the [001] and [110] orientations of MAPbI₃ that was converted at 50 °C. These intergrowths were commonly observed on samples grown in the intermediate temperature range at which both orientations are formed.

The in-plane order of the films is also apparent in the scanning electron microscope (SEM) images in Figure 7. PbO₂ deposits with a needlelike morphology on both the Au(100) and Au(111) substrates. On the Au(100) substrate, the needles are oriented orthogonal to each other (Figure 7a), whereas on the Au(111) substrate, they are rotated 120° relative to each other (Figure 7d). Although all of the MAPbI₃ films also have in-plane order as shown by X-ray pole figures, the most obvious order is seen in the SEM micrographs for the films grown on the Au(100) substrate (Figure 7b,c and Figure S4). The MAPbI₃ consists of rectangular-shaped grains that are oriented orthogonally. For all of the MAPbI₃ films, there is a marked increase in the grain size relative to the electrodeposited PbO₂ films. The MAPbI₃ grains are typically in the size range of 1–5 μm.

The textured and epitaxial films of MAPbI₃ have trap densities lower than and photoluminescence intensities higher than those of polycrystalline films deposited by spin coating PbI₂ and converting it to MAPbI₃. Figure 8a shows the absorption (blue, left axis) and photoluminescence (PL) (red,

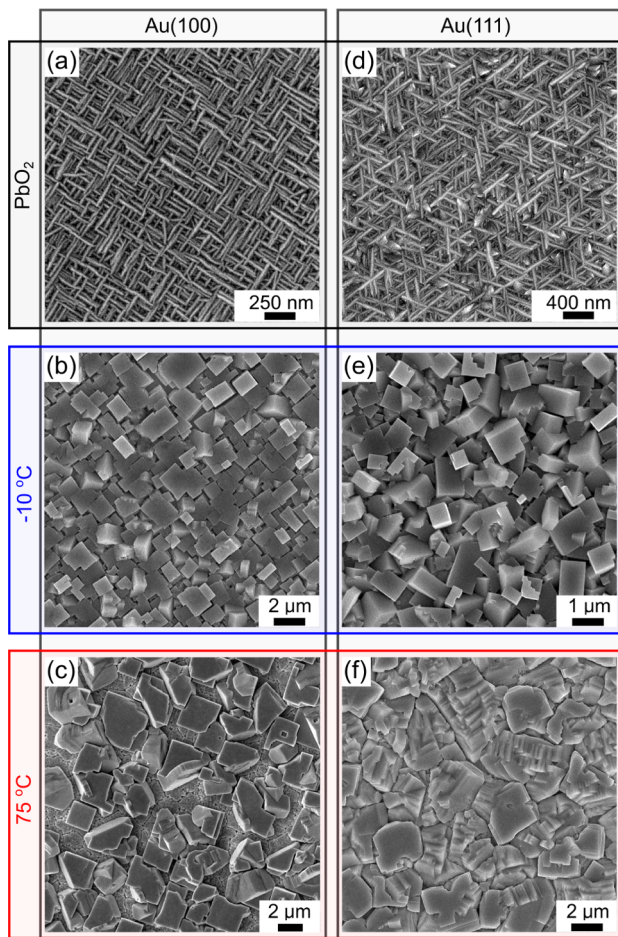


Figure 7. Plan-view SEM images of as-deposited PbO_2 (a and d) and MAPbI_3 films converted at $-10\text{ }^\circ\text{C}$ (b and e) and $75\text{ }^\circ\text{C}$ (c and f) on $\text{Au}(100)$ and $\text{Au}(111)$ substrates.

right axis) spectra of a [110]-textured MAPbI_3 film converted at $75\text{ }^\circ\text{C}$ on Au-coated glass. The absorption spectrum shows a sharp band edge at approximately 760 nm. The band gap determined from absorption is 1.57 eV. A second absorption peak located at approximately 500 nm has been attributed to a double-valence band³⁰ or to a charge-transfer excited state.^{31,32} The PL peak for the film is sharp and close to the band edge with a maximum at 776 nm and a full width at half-maximum of 37 nm, comparable to the PL spectrum reported for large MAPbI_3 single crystals.¹² Figure 8b compares the PL spectra normalized to the material volume for textured (red) and epitaxial (green) MAPbI_3 films and a polycrystalline (blue) MAPbI_3 film produced by conversion of spin-coated PbI_2 (Figure S9). The spectra for the films all exhibit emission peaks at $\sim 780\text{ nm}$, but the peak intensities for the textured and epitaxial films are both approximately 5 times higher than that of the polycrystalline film prepared by conversion of PbI_2 . The PL peak intensity that is higher for the textured and epitaxial films than for the polycrystalline film is consistent with a lower density of traps at grain boundaries that act as nonradiative electron/hole recombination centers.

Because both Au and PbO_2 form ohmic ($\text{PbO}_2/\text{MAPbI}_3/\text{Au}$ cell has a symmetric $I-V$ curve regardless of polarization direction) contacts with MAPbI_3 , it is also possible to directly estimate the trap density from current–voltage curves using space-charge-limited current (SCLC) theory.^{12,13,33} Figure 9

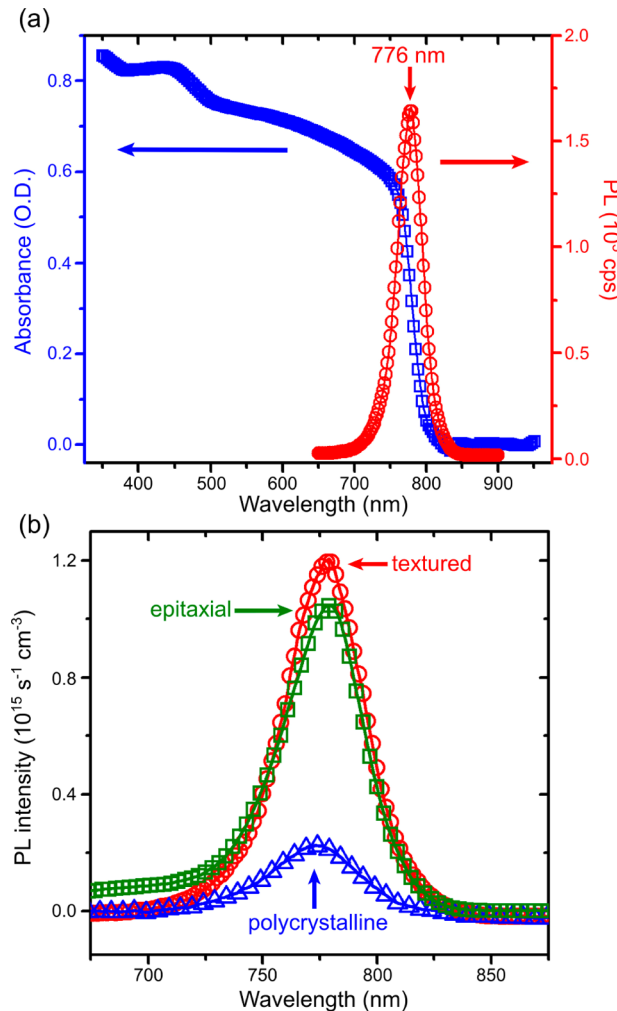


Figure 8. (a) Absorption (blue squares) and photoluminescence (PL) spectra, measured for the [110]-textured MAPbI_3 film converted at $75\text{ }^\circ\text{C}$ on a gold-coated glass substrate. (b) Comparison of PL spectra of the epitaxial (green squares) and [110]-textured (red circles) MAPbI_3 films converted from PbO_2 at $75\text{ }^\circ\text{C}$ and polycrystalline film converted at room temperature from spin-coated PbI_2 (blue triangles). The PL intensity was normalized to the material volume.

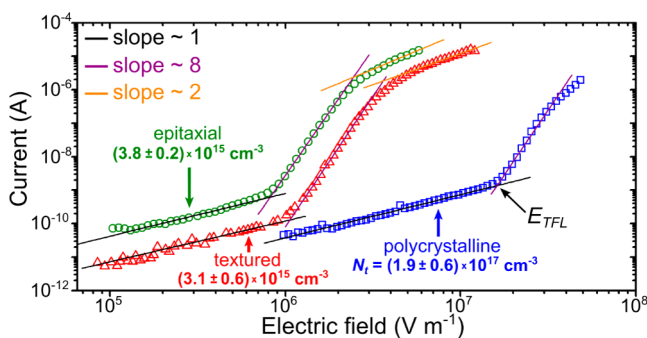


Figure 9. Trap density measurements for the epitaxial MAPbI_3 film converted from PbO_2 at $75\text{ }^\circ\text{C}$ on $\text{Au}(100)$ (green circles), a [110]-textured film converted from PbO_2 at $75\text{ }^\circ\text{C}$ on Au-coated glass (red triangles) substrates, and the polycrystalline film converted at room temperature from spin-coated PbI_2 on a Au-coated glass substrate (blue squares).

compares plots of log(current) versus log(electric field) for an epitaxial $\text{MAPbI}_3(110)$ film converted from PbO_2 at 75 °C on Au(100) (green points), a textured $\text{MAPbI}_3(110)$ film on Au-coated glass (red points), and a polycrystalline MAPbI_3 film converted at room temperature from spin-coated PbI_2 on a Au-coated glass substrate (blue points). All of the films show ohmic behavior at low electric fields (black lines), followed by a sharp increase in current at the trap-filled limit (E_{TFL}). At high electric fields, for the films obtained by conversion of PbO_2 , the current follows a quadratic dependence (orange line) in agreement with the Mott–Gurney law.^{13,30} The trap density, N_t , can be determined from E_{TFL} using eq 1:^{12,13,33}

$$N_t = \frac{2\epsilon\epsilon_0 E_{\text{TFL}}}{eL} \quad (1)$$

where ϵ_0 is the vacuum permittivity, ϵ is the MAPbI_3 dielectric constant (25.5),¹² e is the charge of an electron, and L is the film thickness. The trap densities of the textured and epitaxial films are $(3.8 \pm 0.2) \times 10^{15}$ and $(3.1 \pm 0.6) \times 10^{15} \text{ cm}^{-3}$, respectively, and the trap density in the polycrystalline film is nearly 2 orders of magnitude larger at $(1.9 \pm 0.6) \times 10^{17} \text{ cm}^{-3}$. The same order of magnitude of trap density ($\sim 10^{17} \text{ cm}^{-3}$), determined with time-resolved PL, was reported for polycrystalline perovskite films prepared by single-precursor spin coating.¹⁰ We assume that the epitaxial and textured films have similar trap densities because both films are essentially single crystals along the current path in the trap density measurement. That is, in-plane order is not as important as out-of-plane order for carrier transport in the perovskite films.

CONCLUSIONS

We have shown that textured and epitaxial MAPbI_3 perovskite films can be obtained by an electrochemical/chemical route. The perovskite films are produced by chemical conversion of lead dioxide films that have been electrodeposited as either textured or epitaxial films onto [111]-textured Au and [100] and [111] single-crystal Au substrates. The epitaxial relationships for the MAPbI_3 films are $\text{MAPbI}_3(001)-[010]\parallel\text{PbO}_2(100)\langle 001 \rangle$ and $\text{MAPbI}_3(110)-[111]\parallel\text{PbO}_2(100)\langle 001 \rangle$ regardless of the Au substrate orientation, because the in-plane order of the converted film is controlled by the epitaxial PbO_2 precursor film. The textured and epitaxial MAPbI_3 films both have trap densities lower than and photoluminescence intensities higher than those of polycrystalline films produced by spin coating. The textured films on the inexpensive Au-coated glass substrates should be an ideal morphology for solar cell applications, because there are few or no grain boundaries between the film surface and the substrate that will act as recombination sites. The epitaxial films on single-crystal substrates should provide the preferred platform for determining the intrinsic electronic and optical properties of the perovskites.

ASSOCIATED CONTENT

Supporting Information

The Supporting Information is available free of charge on the ACS Publications website at DOI: [10.1021/acs.chemmater.5b04524](https://doi.org/10.1021/acs.chemmater.5b04524).

Stereographic projections, pole figures for the films produced on Au-coated glass substrates, EDS analysis of the converted film surface and cross section, XRD pattern and surface SEM images of the MAPbI_3 film

produced by spin coating, and additional characterization data ([PDF](#))

AUTHOR INFORMATION

Corresponding Author

*E-mail: jswitzer@mst.edu.

Notes

The authors declare no competing financial interest.

ACKNOWLEDGMENTS

This work was supported by the U.S. Department of Energy, Office of Basic Sciences, under Grant DE-FG02-08ER46518.

REFERENCES

- Kojima, A.; Teshima, K.; Shirai, Y.; Miyasaka, T. Organometal Halide Perovskites as Visible-Light Sensitizers for Photovoltaic Cells. *J. Am. Chem. Soc.* **2009**, *131*, 6050–6051.
- Snaith, H. J. Perovskites: The Emergence of a New Era for Low-Cost, High-Efficiency Solar Cells. *J. Phys. Chem. Lett.* **2013**, *4*, 3623–3630.
- Green, M. A.; Ho-Baillie, A.; Snaith, H. J. The emergence of perovskite solar cells. *Nat. Photonics* **2014**, *8*, 506–514.
- Kim, H.-S.; Im, S. H.; Park, N.-G. Organolead Halide Perovskite: New Horizons in Solar Cell Research. *J. Phys. Chem. C* **2014**, *118*, 5615–5625.
- Gao, P.; Gratzel, M.; Nazeeruddin, M. K. Organohalide lead perovskites for photovoltaic applications. *Energy Environ. Sci.* **2014**, *7*, 2448–2463.
- Burschka, J.; Pellet, N.; Moon, S.-J.; Humphry-Baker, R.; Gao, P.; Nazeeruddin, M. K.; Gratzel, M. Sequential deposition as a route to high-performance perovskite-sensitized solar cells. *Nature* **2013**, *499*, 316–319.
- Liu, M.; Johnston, M. B.; Snaith, H. J. Efficient planar heterojunction perovskite solar cells by vapour deposition. *Nature* **2013**, *501*, 395–398.
- National Center for Photovoltaics at the National Renewable Energy Laboratory. Research cell efficiency records. www.nrel.gov/ncpv/ (August 6, 2015, revision).
- Liang, K.; Mitzi, D. B.; Priks, M. T. Synthesis and Characterization of Organic–Inorganic Perovskite Thin Films Prepared Using a Versatile Two-Step Dipping Technique. *Chem. Mater.* **1998**, *10*, 403–411.
- Noel, N. K.; Abate, A.; Stranks, S. D.; Parrott, E. S.; Burlakov, V. M.; Goriely, A.; Snaith, H. J. Enhanced Photoluminescence and Solar Cell Performance via Lewis Base Passivation of Organic–Inorganic Lead Halide Perovskites. *ACS Nano* **2014**, *8*, 9815–9821.
- Eperon, G. E.; Burlakov, V. M.; Docampo, P.; Goriely, A.; Snaith, H. J. Morphological Control for High Performance, Solution-Processed Planar Heterojunction Perovskite Solar Cells. *Adv. Funct. Mater.* **2014**, *24*, 151–157.
- Shi, D.; Adinolfi, V.; Comin, R.; Yuan, M.; Alarousu, E.; Buin, A.; Chen, Y.; Hoogland, S.; Rothenberger, A.; Katsiev, K.; Losovyj, Y.; Zhang, X.; Dowben, P. A.; Mohammed, O. F.; Sargent, E. H.; Bakr, O. M. Low trap-state density and long carrier diffusion in organolead trihalide perovskite single crystals. *Science* **2015**, *347*, 519–522.
- Dong, Q.; Fang, Y.; Shao, Y.; Mulligan, P.; Qiu, J.; Cao, L.; Huang, J. Electron-hole diffusion lengths > 175 μm in solution-grown $\text{CH}_3\text{NH}_3\text{PbI}_3$ single crystals. *Science* **2015**, *347*, 967–970.
- Nie, W.; Tsai, H.; Asadpour, R.; Blancon, J.-C.; Neukirch, A. J.; Gupta, G.; Crochet, J. J.; Chhowalla, M.; Tretiak, S.; Alam, M. A.; Wang, H.-L.; Mohite, A. D. High-efficiency solution-processed perovskite solar cells with millimeter-scale grains. *Science* **2015**, *347*, 522–525.
- deQuilettes, D. W.; Vorpahl, S. M.; Stranks, S. D.; Nagaoka, H.; Eperon, G. E.; Ziffer, M. E.; Snaith, H. J.; Ginger, D. S. Impact of microstructure on local carrier lifetime in perovskite solar cells. *Science* **2015**, *348*, 683–686.

- (16) Yang, W. S.; Noh, J. H.; Jeon, N. J.; Kim, Y. C.; Ryu, S.; Seo, J.; Seok, S. I. High-performance photovoltaic perovskite layers fabricated through intramolecular exchange. *Science* **2015**, *348*, 1234–1237.
- (17) Stoumpos, C. C.; Malliakas, C. D.; Kanatzidis, M. G. Semiconducting Tin and Lead Iodide Perovskites with Organic Cations: Phase Transitions, High Mobilities, and Near-Infrared Photoluminescent Properties. *Inorg. Chem.* **2013**, *52*, 9019–9038.
- (18) Li, Y.; Wang, X.; Wu, S.; Ci, H.; Xu, H.; Li, X.; Sun, H.; Zhang, Z.; Cao, A.; Guo, X.; Li, Y. Large-scale aligned crystalline $\text{CH}_3\text{NH}_3\text{PbI}_3$ perovskite array films. *J. Mater. Chem. A* **2015**, *3*, 18847–18851.
- (19) Hill, J. C.; Koza, J. A.; Switzer, J. A. Electrodeposition of Epitaxial Lead Iodide and Conversion to Textured Methylammonium Lead Iodide Perovskite. *ACS Appl. Mater. Interfaces* **2015**, *7*, 26012–26016.
- (20) Vertegel, A. A.; Bohannan, E. W.; Shumsky, M. G.; Switzer, J. A. Epitaxial Electrodeposition of Orthorhombic $\alpha\text{-PbO}_2$ on (100)-Oriented Single Crystal Au. *J. Electrochem. Soc.* **2001**, *148*, C253–C256.
- (21) Baikie, T.; Fang, Y.; Kadro, J. M.; Schreyer, M.; Wei, F.; Mhaisalkar, S. G.; Graetzel, M.; White, T. J. Synthesis and crystal chemistry of the hybrid perovskite $(\text{CH}_3\text{NH}_3)\text{PbI}_3$ for solid-state sensitised solar cell applications. *J. Mater. Chem. A* **2013**, *1*, 5628–5641.
- (22) Switzer, J. A.; Shumsky, M. G.; Bohannan, E. W. Electro-deposited Ceramic Single Crystals. *Science* **1999**, *284*, 293–296.
- (23) Switzer, J. A.; Kothari, H. M.; Poizot, P.; Nakanishi, S.; Bohannan, E. W. Enantiospecific electrodeposition of a chiral catalyst. *Nature* **2003**, *425*, 490–493.
- (24) Bohannan, E. W.; Shumsky, M. G.; Switzer, J. A. Epitaxial Electrodeposition of Copper(I) Oxide on Single-Crystal Gold(100). *Chem. Mater.* **1999**, *11*, 2289–2291.
- (25) Limmer, S. J.; Kulp, E. A.; Switzer, J. A. Epitaxial Electro-deposition of ZnO on Au(111) from Alkaline Solution: Exploiting Amphotericism in Zn(II). *Langmuir* **2006**, *22*, 10535–10539.
- (26) Boonsalee, S.; Gudavarthy, R. V.; Bohannan, E. W.; Switzer, J. A. Epitaxial Electrodeposition of Tin(II) Sulfide Nanodisks on Single-Crystal Au(100). *Chem. Mater.* **2008**, *20*, 5737–5742.
- (27) Kim, H.-S.; Lee, C.-R.; Im, J.-H.; Lee, K.-B.; Moehl, T.; Marchioro, A.; Moon, S.-J.; Humphry-Baker, R.; Yum, J.-H.; Moser, J. E.; Gratzel, M.; Park, N.-G. Lead Iodide Perovskite Sensitized All-Solid-State Submicron Thin Film Mesoscopic Solar Cell with Efficiency Exceeding 9%. *Sci. Rep.* **2012**, *2*, 591.
- (28) Chen, H.; Wei, Z.; Zheng, X.; Yang, S. A scalable electrodeposition route to the low-cost, versatile and controllable fabrication of perovskite solar cells. *Nano Energy* **2015**, *15*, 216–226.
- (29) Docampo, P.; Hanusch, F. C.; Giesbrecht, N.; Angloher, P.; Ivanova, A.; Bein, T. Influence of the orientation of methylammonium lead iodide perovskite crystals on solar cell performance. *APL Mater.* **2014**, *2*, 081508.
- (30) Xing, G.; Mathews, N.; Sun, S.; Lim, S. S.; Lam, Y. M.; Grätzel, M.; Mhaisalkar, S.; Sum, T. C. Long-Range Balanced Electron- and Hole-Transport Lengths in Organic-Inorganic $\text{CH}_3\text{NH}_3\text{PbI}_3$. *Science* **2013**, *342*, 344–347.
- (31) Stamplecoskie, K. G.; Manser, J. S.; Kamat, P. V. Dual nature of the excited state in organic-inorganic lead halide perovskites. *Energy Environ. Sci.* **2015**, *8*, 208–215.
- (32) Christians, J. A.; Miranda Herrera, P. A.; Kamat, P. V. Transformation of the Excited State and Photovoltaic Efficiency of $\text{CH}_3\text{NH}_3\text{PbI}_3$ Perovskite upon Controlled Exposure to Humidified Air. *J. Am. Chem. Soc.* **2015**, *137*, 1530–1538.
- (33) Bube, R. H. Trap Density Determination by Space-Charge-Limited Currents. *J. Appl. Phys.* **1962**, *33*, 1733–1737.